A modifed Halpin–Tsai model for the tensile properties of short fber-reinforced 3D-printed composites using fber content-dependent orientation correction factor

Tóth Cs., Virág Á. D.

Accepted for publication in International Journal of Advanced Manufacturing Technology
Published in 2025
DOI: https://doi.org/10.1007/s00170-025-15738-x

The International Journal of Advanced Manufacturing Technology
https://doi.org/10.1007/s00170-025-15738-x

ORIGINAL ARTICLE

A modified Halpin–Tsai model for the tensile properties of short fiber-reinforced 3D-printed composites using fiber content-dependent orientation correction factor

Csenge Tóth[1,2] · **Ábris Dávid Virág**[1]

Received: 27 February 2025 / Accepted: 8 May 2025

Abstract
This study investigates the applicability of micromechanical models for predicting the mechanical properties of short fiber-reinforced 3D-printed composites. Basalt fiber-reinforced poly(lactic acid) composites are analyzed by microstructural measurements to determine fiber length and fiber orientation factors. Micro-computed tomography analysis identifies a linear relationship between fiber content and fiber orientation, enabling an improved method for estimating the fiber orientation correction factor. The application of this correction allows the prediction of Young's modulus and tensile strength while reducing the number of measurements required. The modified Halpin–Tsai model shows high accuracy, with an average error of 7% for Young's modulus and 18% for tensile strength for fiber contents ranging from 5 to 25 w%. In addition, an anisotropy ratio was introduced as a dimensionless parameter to quantify the directional dependence of the tensile properties. Since 3D-printed fiber-reinforced composites are commonly used in load-bearing structures, understanding their anisotropic behavior is essential for optimal component design. These results contribute to improving the predictability of mechanical properties, supporting the efficient design of 3D-printed composite parts for engineering applications.

Keywords Micro-computed tomography · Micromechanical modeling · Short fiber · Polymer composites · Microstructure

1 Introduction

Short fiber-reinforced composites (SFRCs) are widely used in the automotive, aerospace, and biomedical industries due to their enhanced mechanical properties and lightweight and cost-effective manufacturing [1, 2]. The advent of 3D printing technologies has further expanded their applicability, enabling customized geometries and controlled orientation of fibers. The mechanical behavior of 3D-printed SFRCs is strongly influenced by their microstructural features, such as the fiber length, fiber orientation, and the fiber-matrix adhesion [3, 4]. These microstructural features depend on the manufacturing process and thus have little predictability in the product [5, 6].

The fiber orientation is determined by the printing direction due to shear. It is also assumed that the filament fabrication process has aligned the majority of the fibers along the length [7]. The type of fiber affects orientation, as stiffer fibers may fragment and inhibit each other's movement more than flexible fibers [8, 9]. Consul et al. [10] and Yan et al. [11] found that the nozzle diameter has the strongest effect on orientation so narrower diameters cause a higher degree of fiber alignment. This result is expected, as forcing the same material flow through a narrower space increases shear, causing the fibers to align in the direction of the highest shear. Shulga et al. [12] also found that layer height has the same effect on orientation, for the same reasons.

The quality of interfacial adhesion can be evaluated using the critical fiber length—the minimum fiber length required to effectively transfer stress and provide tensile reinforcement within a given fiber/matrix system. In the case of 3D-printed short fiber-reinforced composites, only a few research articles can be found on the subject of adhesion and fiber length. Yu et al. [13] found that 3D-printed

✉ Csenge Tóth
tothcs@pt.bme.hu

[1] Department of Polymer Engineering, Faculty of Mechanical Engineering, Budapest University of Technology and Economics, Műegyetem Rkp. 3, 1111 Budapest, Hungary

[2] MTA-BME Lendület Lightweight Polymer Composites Research Group, Műegyetem Rkp. 3, 1111 Budapest, Hungary

Published online: 21 May 2025

composites show distinctive mechanical behavior under different adhesion conditions. The authors observed that strong adhesion led to increased tensile strength and enhanced toughness, the latter attributed to void formation. Papon et al. [14] applied oxidation treatment on carbon fibers to increase bonding with poly(lactic) acid matrix. Better bonding also reduced micro-voids at the fiber interface.

3D-printed structures are anisotropic, which means that there can be a large difference (even an order of magnitude) between in-plane mechanical properties and those perpendicular to the printing direction. Numerous studies investigated interlayer bonding in the case of neat polymers. However, the effect of fibers is less explored. The highest value found in the literature was achieved by Allum et al. [15], who state that poor interlayer properties are not due to insufficient polymer bonding but due to geometric features. However, their claim contradicts other literature and may require further verification. König et al. [16] investigated the effects of process parameters on the interlayer bonding of carbon fiber–reinforced polyamide composites. The authors found that carbon fibers decrease interlayer bonding strength, probably due to weak fiber-matrix adhesion. Bhandari et al. [17] found that carbon fibers reduce the interlayer tensile strength by 66% and 50% for an amorphous and a semi-crystalline polymer, respectively. Post-processing increases strength but also increases production time and can deform 3D-printed products. The authors reported that increased melt viscosity and crystallization inhibit diffusion between layers and can therefore result in poor interlayer bond strength.

PLA is widely used for 3D printing because of its relatively low processing temperature range and low shrinkage. It can be produced from renewable resources and is biodegradable, thus meeting the sustainable management guidelines of industry and EU regulations. With the addition of reinforcing fibers, it can also be used for engineering purposes. As basalt is natural, PLA composites reinforced with basalt fibers (BF) have the potential to be a more sustainable thermoplastic composite alternative for semi-industrial applications. BF/PLA composites are also biologically inert, so have application possibilities in the medical sector [18, 19].

The aim of this study is to advance the micromechanical modeling methods for 3D-printed short fiber composites by evaluating the applicability of correction factors. These factors are typically derived from extensive microstructural measurements, which can be time-consuming. To address this issue, we explore the potential of micro-computed tomography to identify correlations within the internal structure. This study is particularly relevant for mechanical engineers and designers working with fiber-reinforced composites, as the proposed approach enables faster and more cost-effective material characterization. It complements the state of the art by offering a practical, data-driven alternative to time-consuming orientation measurements.

2 Materials and methods

2.1 Preparation of composite filaments

As the matrix of the composites, Ingeo 4060D poly(lactic) acid (PLA) from Natureworks LLC (USA) was used. Chopped basalt fibers (KV-18) were obtained from Kamenny Vek (Russia). The fibers were cut from a continuous yarn and sized for compounds based on polypropylene and polyethylene. The nominal fiber diameter is 12 µm and the initial fiber length is 10 mm. The density of the basalt fibers is 2.59 g/cm^3, the tensile strength is 2335 MPa, and the Young's modulus is 85 GPa [20–22]. The density and mechanical properties of the constituents were used to calculate the mechanical properties of the composites. The PLA pellets were dried for 4 h at 45 °C before processing in a WGLL-125 BE drying oven from Faithful Instrument Co., LTD (China).

Figure 1 presents the main processing steps and the corresponding parameters. First, the dry mixtures were prepared in the appropriate weight ratios (5, 10, 15, 20, 25 w%). Then, the mixtures were fed to a twin-screw extruder (LTE 26–44 manufactured by Labtech Engineering Co., Ltd., Thailand). The screw diameter and the L/D ratio were 26 mm and 44, respectively. The zone temperatures from hopper to die were 180 °C, 190 °C, 190 °C, 190 °C, 190 °C, 200 °C, 200 °C, 200 °C, 200 °C, 200 °C, and 190 °C.

After compounding, the composite extrudates were cut into 6-mm long pellets with a LZ-120/VS granulator from Labtech Engineering Co., Ltd. (Thailand). Then, the pellets were fed to a single-screw filament extruder (Precision 450, 3devo Inc., The Netherlands) to prepare the filaments for 3D printing. Screw speed (r) was 4.5 rpm and the zone temperatures from hopper to die were 170 °C, 210 °C, 185 °C, and 175 °C. Filament diameter was 1.7 ± 0.5 mm. The filament extruder is equipped with a winding and spooling system, and the diameter is automatically controlled based on live data acquisition. During extrusion, the diameter of the material exiting the die is constantly measured via a sensor, and the pulling rate is adjusted accordingly. Neat PLA filaments were also produced with the same process to ensure the same manufacturing history of the materials.

2.2 3D printing of the samples

Two types of specimens were fabricated for tensile testing. To evaluate in-plane tensile properties, the 5 A-type geometry was used as specified in ISO 527–2:2012. These specimens were printed flat on the print bed, with the printing

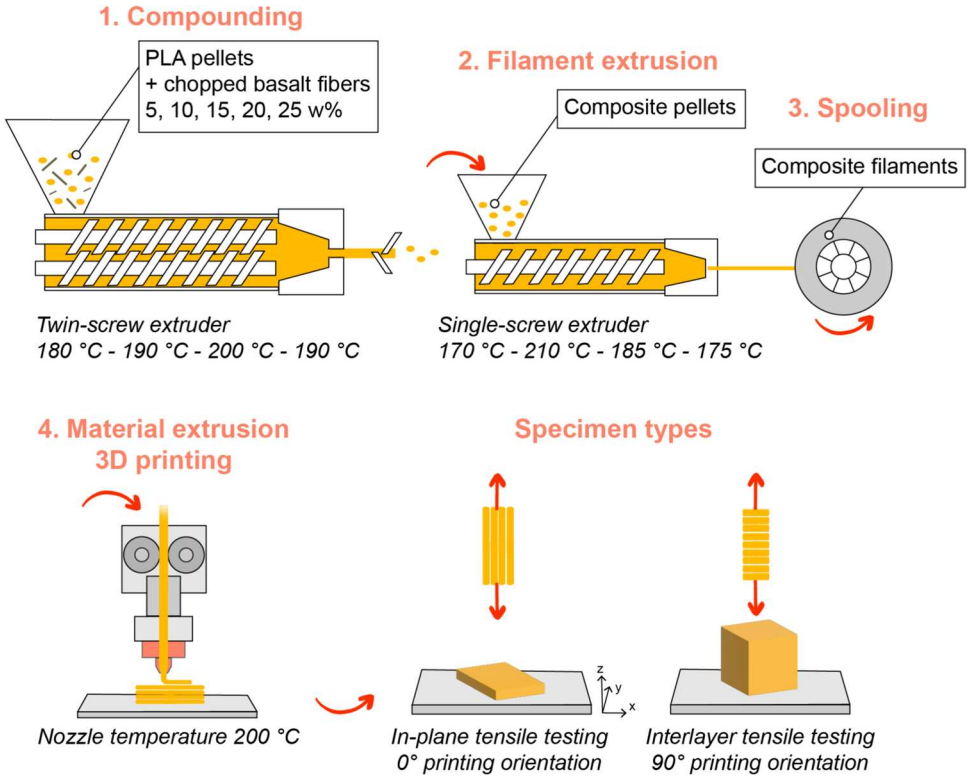

Fig. 1 Steps of the filament preparation method and the specimens for in-plane tensile testing (0° printing orientation) and interlayer tensile testing (90° printing orientation)

orientation aligned parallel (0°) to the longitudinal axis in each layer. For interlayer tensile property measurements, a custom specimen was designed [23]. Hollow boxes were printed with a single contour, then rectangular specimens were cut using lever plate shears. The wall thickness was 0.8 mm. Tensile testing was conducted with the load applied perpendicular to the build direction, allowing the assessment of interlayer adhesion. Schematics of the samples are shown in Fig. 1. The 25 w% basalt fiber–reinforced filament was not suitable due to its brittleness. All samples were prepared using a Craftbot + desktop FFF printer (Craftbot, Hungary). The G-codes were generated with Ultimaker Cura 4.13.1 (Ultimaker B.V., The Netherlands). Printing parameters included a 0.8-mm nozzle diameter, 200 °C nozzle temperature, 0.2 mm layer height, and 100% infill rate. The print bed was heated to 60 °C, and fan cooling was not used.

2.3 Tensile testing

The in-plane and the interlayer tensile properties were determined with a Zwick Z005 (Zwick Roell AG, Germany) universal testing machine in accordance with the ISO 527 standard, with a crosshead speed of 5 mm/min, at 25 °C and in 20% relative humidity. Twenty kN-rated Zwick 8131 screw grips were used. The gripping distance was 50 mm. At least 5 specimens were tested in each case. Young's modulus (E) was determined as a chord slope between 0.05% and 0.25% strains. The ultimate tensile strength was given with Eq. 1.

$$\sigma_{exp,xy} = \frac{F}{A_{xy}} \; and \; \sigma_{exp,z} = \frac{F}{A_z} \tag{1}$$

where $\sigma_{exp,xy}$(MPa) denotes the experimental in-plane tensile strength and A_{xy}(mm) is the cross-section in the (x, y) plane. $\sigma_{exp,z}$(MPa) is the experimental interlayer tensile strength and A_z(mm) is the cross-section of the single-wall specimens. The cross-sections were calculated as follows:

$$A_{xy} = h_1 b_1 \; and \; A_z = h_2 b_2 \tag{2}$$

where $h_1 = 4$mm, $b_1 = 2$ mm, and $h_2 = 5$ mm, $b_2 = 0.8$mm.

2.4 Microstructure

Micro-computed tomography (micro-CT) measurements were performed to qualify the fiber orientation after 3D printing. Samples with a size of 4 × 2 × 5 mm were cut from the middle of the 3D-printed specimens, and a GE Phoenix Micromex 180 PCB (Baker Hughes Company, Houston) X-ray device was applied to acquire data. Figure 2 shows representative cross-sections from micro-CT analysis. The samples were rotated 360° while being exposed to an X-ray beam (accelerating voltage 180 kV; power 20 W). Then, the 3D geometry was reconstructed with Volume Graphics Studio Max software. Phases in the

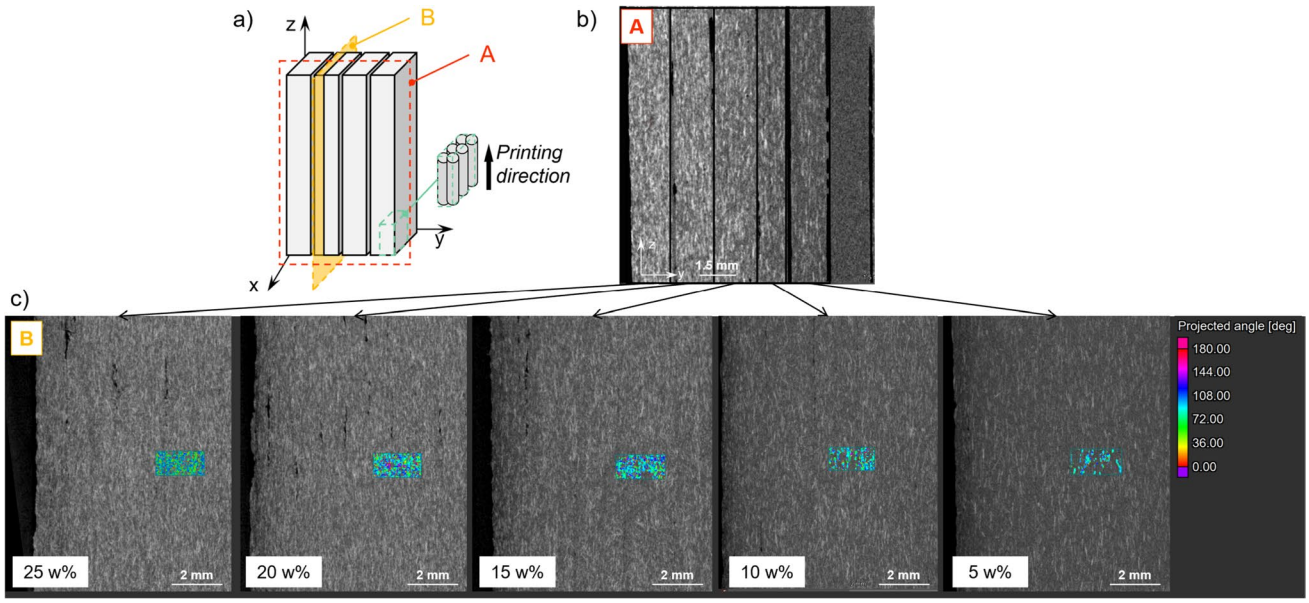

Fig. 2 Representative cross-sections of the samples used for micro-CT analysis: (**a**) schematic representation of the sample preparation process for micro-CT, (**b**) longitudinal cross-section along the thickness, (**c**) longitudinal cross-section along the width

composites were segmented with gray level values based on the density differences of the materials. 3D fiber orientation angle and the tensor components were determined using fiber composite material analysis. The second-order fiber orientation tensor (A_{ij}) is given with Eq. 3. The fiber orientation distribution (h(θ)) was approximated with two-term Gaussian distribution function, given by Eq. 4.

$$A_{ij} = \begin{bmatrix} a_{xx} & a_{xy} & a_{xz} \\ a_{yx} & a_{yy} & a_{yz} \\ a_{zx} & a_{zy} & a_{zz} \end{bmatrix} \tag{3}$$

$$h(\theta) = \alpha_1 e^{-\left(\frac{\theta-\beta_1}{\gamma_1}\right)^2} + \alpha_2 e^{-\left(\frac{\theta-\beta_2}{\gamma_2}\right)^2} \tag{4}$$

where θ is the polar angle; α_1, α_2, β_1, β_2, γ_1, and γ_2 are fitted constants.

The fiber length (L) is expected to decrease due to the two-step processing. To measure the fiber length, 3-g pieces were cut from the samples and placed in a Denkal 5B furnace at 600 °C for 4 h. This removed the matrix material. Then, the fibers were dispersed on glass sheets and the individual lengths were measured with a Keyence VHX-5000 (Keyence Corporation, Mechelen) digital optical microscope with ×40 magnification. At least 300 fibers were measured in all cases. The numerical averages (L_n) were measured according to Eq. 5, and the length-weighted averages (L_w) with Eq. 6.

$$L_n = \frac{\sum n_i L_i}{\sum n_i} \tag{5}$$

$$L_w = \frac{\sum n_i L_i^2}{\sum n_i L_i} \tag{6}$$

where L_i (μm) is the length of *i*th fiber, n_i is the number of fibers having L_i length, and *n* is the total number of fibers.

The fiber length distribution (f(L)) was approximated with the Weibull distribution function according to Eq. 7.

$$f(L|a,b) = b/a(L/a)^{b-1} e^{-(L/a)^b} \text{ if } L \geq 0 \tag{7}$$

where *a* and *b* are the fitted scale and shape parameters, respectively.

Lastly, to gain more insight into the microstructure of the composites, the broken surfaces of the specimens were analyzed after tensile testing using a JSM 6380LA scanning electron microscope from Jeol Ltd. (Japan). Before image acquisition, the samples were sputtered with gold.

2.5 Micromechanical modeling

Micromechanical and homogenization models are mathematical frameworks used to predict the macroscopic properties based on the microstructural features of the composite. Micromechanical models aim to describe the

effective properties by considering the behavior of an individual fiber within the matrix, and homogenization models are techniques used to bridge the microstructure and macroscopic behavior by averaging the material properties. Both require high-precision input parameters, which can be determined by quantifying the individual microstructural features. In this study, the rule of mixture (RoM) and the semi-empirical Halpin–Tsai (H-T) models were applied to estimate the in-plane tensile properties. A generalized method for micromechanical modeling of short fiber-reinforced composites is shown in Fig. 3. Micromechanical and homogenization models require detailed knowledge of microstructural parameters such as fiber length, orientation, and void content. These characteristics are typically measured using imaging techniques such as optical microscopy or 3D imaging. After data processing, mathematical descriptors are generated to represent microstructural properties for modeling. Such parameters are the fiber length correction factor calculated from the fiber length distribution, or the orientation correction factor calculated from the Gaussian function describing the 2D fiber alignment. In addition, the models require inherent material properties as input, such as bulk modulus, density, and tensile strength. In 3D-printed short fiber-reinforced composites, reinforcing and toughening mechanisms operate at both the micro and macro levels [24]. At the micro level, mechanisms such as fiber bridging, fiber pull-out, and crack deflection play a dominant role. When short fibers are well aligned and evenly distributed, they can connect developing cracks and transfer the load, which can improve fracture toughness. Fiber pullout, which occurs due to crack propagation, dissipates a significant amount of energy, contributing to improved toughness. The deflection of cracks around the fibers also increases the fracture surface and the energy required for crack growth [25]. In addition, a strong interfacial bond between the fibers and the matrix is essential for efficient stress transfer. At the macroscopic level, the anisotropic nature of 3D printing can result in additional toughening due to the alignment of the fibers in the printing direction. The porosity of 3D printed structures and the interlayer bonding also significantly influence the macroscopic behavior.

The simplest model for estimating the tensile strength of a composite is the rule of mixture (RoM), which takes into account the tensile strength of the constituents and their weight or volume ratio (Eq. 8). It is assumed that the fibers are perfectly aligned in the load direction, the load transfer between the matrix and the fibers is perfect, and both fiber and matrix are linearly elastic under applied loads.

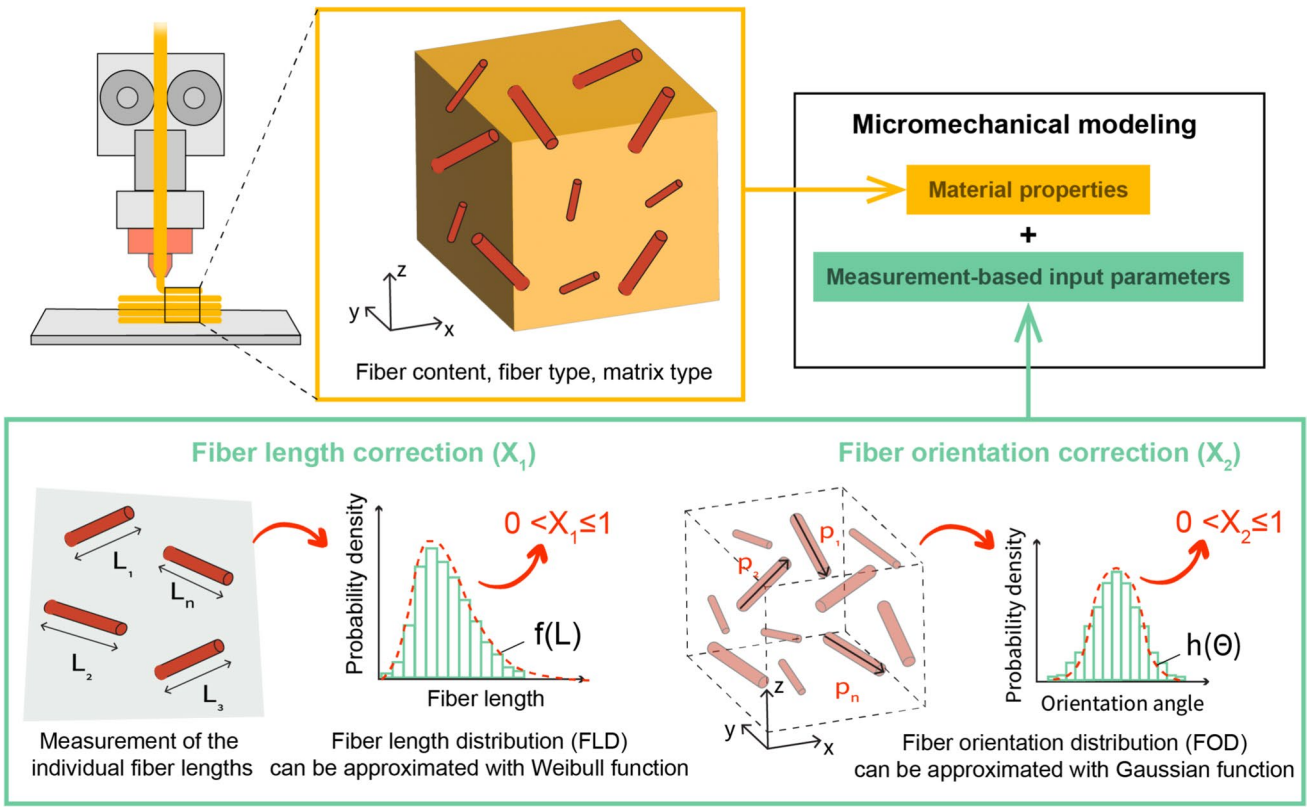

Fig. 3 Input parameters for the micromechanical modeling of short fiber-reinforced 3D-printed composites

$$\sigma_{ROM} = w_f\sigma_f + w_m\sigma_m \tag{8}$$

where σ and w are the tensile strength and the weight fraction, respectively. The subscripts "f" and "m" denote fiber and matrix, respectively.

In a modified version of the Halpin–Tsai (H-T) model for tensile strength, the fiber length and the fiber orientation distribution are incorporated with correction factors (Eq. 9):

$$\sigma_{HT} = \chi_1\chi_2\sigma_f w_f + w_m\sigma_m \tag{9}$$

where χ_1 is the fiber length correction factor and χ_2 is the fiber orientation correction factor. The fiber length correction factor (χ_1) can be calculated using Eq. 10 [26].

$$\chi_1 = \int_{L_{min}}^{L_{crit}} \left[L^2/2L_{crit}L_n\right] f(L)dL + \int_{L_{crit}}^{L_{max}} \left(\frac{L}{L_n}\right)\left[1 - \frac{L_{crit}}{2L}\right] f(L)dL \tag{10}$$

where L_n (mm) is the number average fiber length, L_{crit} (mm) is the estimated critical fiber length, L_{min} and L_{max} (mm) are the shortest and the longest fibers measured, respectively, and f(L) is the fiber length distribution. The L_{min}, L_{max}, L_n, and the f(L) were determined on burnt-out samples using optical microscopy, described in Sect. 2.4. The L_{crit} was determined according to our previous study [20]. During the calculation of χ_1, the critical fiber length (L_{crit}) is taken into account, which is dependent on the fiber-matrix adhesion. However, its value is rarely determined experimentally, so inaccuracy should be expected. χ_1 depends on the number average fiber length (L_n) and the critical fiber length (L_{crit}) and can be obtained by integrating the area under the fiber length distribution function. Therefore, the distribution must be determined experimentally, and then a suitable continuous function must be used to describe it. Predictive methods to estimate the fiber length distribution after processing are scarce. Most methods contain experimental constants, which are production and material-specific values, making them difficult to generalize [27, 28]. In summary, the determination of the fiber length correction factor requires measurements of the samples produced, which calls into question the predictive value of its application.

The fiber orientation correction factor (χ_2) can be given with Eq. 11 [29]. Similarly to length, it can be derived from the area under the distribution curves.

$$\chi_2 = \int_0^{\pi/2} h(\theta)\cos\theta d\theta \times \int_0^{\pi/2} h(\theta)(cos^3\theta - \nu sin^2\theta cos\theta)d\theta \tag{11}$$

where ν is the Poisson ratio, θ is the polar angle, and h(θ) is the fiber orientation distribution. The h(θ) distributions were obtained from micro-CT measurements, described in Sect. 2.4. For Poisson's ratio, the contraction perpendicular to the fibers as a result of extension parallel to the fibers with a value of ν=0.33 was used in all cases [30]. Note that the H-T model for tensile strength is consistent with the RoM model when $\chi_1 = 1$, i.e., all fibers are infinite length (continuous fibers), and $\chi_2 = 1$, i.e., all fibers aligned in the printing direction (unidirectional fibers). When using the H-T model, homogeneous stress distribution and uniform fiber distribution are assumed. These can also lead to overestimation, as fiber clustering and agglomeration can occur with higher fiber contents or if fiber dispersion during processing has not been fully successful. Overall, micromechanical models are expected to be less accurate for strength predictions as strength is a failure property that depends on damage mechanisms, defects, and random variables.

To estimate the Young's modulus (E), the RoM model (Eq. 12) was also used in the simplest case. Micromechanical models are generally more accurate for elastic modulus than for strength, as the stiffness depends on deformation under small strains. Under small strains, the effects of defects such as partial load transfer or voids are usually negligible.

$$E_{ROM} = w_f E_f + w_m E_m \tag{12}$$

To obtain more accurate predictions, correction factors can also be applied. The H-T model for Young's modulus (Eq. 13) incorporates the reinforcing efficiency and the fiber geometry [26, 31].

$$E_{HT} = E_m\left(\frac{1 + \xi\eta w_f}{1 - \eta w_f}\right) \tag{13}$$

where η is the reinforcing efficiency and ξ is the empirical shape factor. The η expresses the relative stiffness improvement due to the reinforcement (Eq. 14) [26, 31].

$$\eta = \frac{E_f - E_m}{E_f + \xi E_m} \tag{14}$$

To obtain longitudinal modulus for circular fibers, the shape factor was calculated with Eq. 15 [26].

$$\xi = 2(L_n/D) \tag{15}$$

where L_n is the number average fiber length and D is the fiber diameter. These values were determined from optical microscopy measurements, as described in Sect. 2.4.

To qualify the goodness of the model predictions, the percent error (δ) was calculated in every case using Eq. 16.

$$\delta(\%) = \left|\frac{X_{measured} - X_{pred}}{X_{measured}}\right| \cdot 100 \tag{16}$$

where X stands for tensile strength or Young's modulus and the subscripts "measured" and "pred" stand for the measured properties and the model prediction values, respectively.

2.6 Characterization of 3D anisotropy

It is long established in the literature that 3D-printed structures are anisotropic. 3D printed products are typically not shell elements but components with non-negligible thickness. For short fiber-reinforced 3D-printed composites, the typical application is more similar to injection molded products rather than laminated composites. Therefore, for structures designed for complex loading, it is important to know the degree of anisotropy as a function of the composite properties.

The degree of directional dependence of the tensile properties, namely the ultimate tensile strength, elongation at break, and Young's modulus, was also investigated. An anisotropy ratio was defined using in-plane and interlayer test results. The anisotropy ratio (ϑ) is a dimensionless parameter that expresses the degree of directional dependence of a given mechanical property, where 1 represents isotropic behavior. If $0 < \vartheta \leq 1$, the mechanical property is higher in (x, y) plane, and if $\vartheta > 1$, it is higher in the z direction. The anisotropy ratio for tensile strength, Young's modulus, and the elongation at break is given with Eqs. 17, 18, and 19, respectively.

$$\vartheta_{\sigma} = \frac{\sigma_z}{\sigma_{xy}} \tag{17}$$

$$\vartheta_{E} = \frac{E_z}{E_{xy}} \tag{18}$$

$$\vartheta_{\varepsilon} = \frac{\varepsilon_z}{\varepsilon_{xy}} \tag{19}$$

where $\sigma_z(MPa), E_z(GPa)$, and$\varepsilon_z(-)$ are the interlayer; and $\sigma_{xy}(MPa), E_{xy}(GPa)$, and $\varepsilon_{xy}(-)$ are the in-plane tensile strength, Young's modulus, and elongation at break, respectively.

3 Results and discussion

3.1 Fiber length distribution

Figure 4 shows the obtained fiber length distributions and the calculated number- (L_n) and length-weighted average fiber length (L_w) values. The average fiber length values show a decreasing trend, with increasing fiber content, indicating an increase in fiber–fiber interactions and

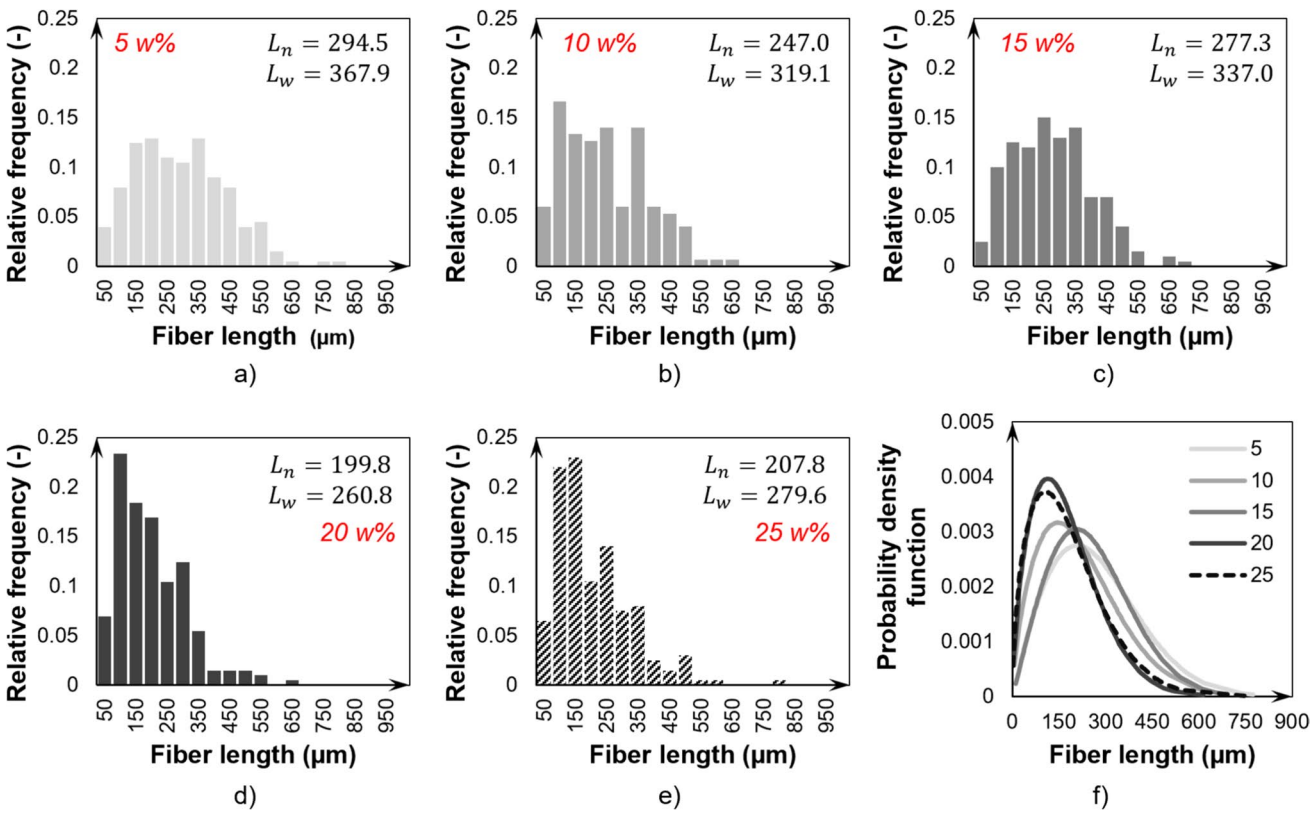

Fig. 4 Fiber length distributions of composites with different fiber contents: **a**) 5 w%, **b**) 10 w%, **c**) 15 w%, **d**) 20 w%, **e**) 25 w%, **f**) probability density functions

shear-induced breakage during compounding and 3D printing (Fig. 4a–e). To rate the change in fiber length distribution as a function of fiber content, we fitted the Weibull distribution function (Eq. 7) on all the fiber length data (Fig. 4f). These distributions were used to calculate the fiber length correction factors (χ_1) for tensile strength predictions. Generally, the distributions shifted towards shorter lengths as fiber content increased. The horizontal displacement of the peak maximum between the lowest and the highest fiber contents was 84 µm. This shows that the effect of fiber content on fiber length was minor overall.

In the literature, the average fiber length is between 100 and 500 µm, but very short fiber lengths of less than 100 µm can also be found [32]. By comparison, it is common to produce products with an average fiber length of more than 1 mm with other thermoplastic composite processing technologies, e.g., injection molding or compression molding [33, 34]. In the case of 3D printing, producing composites with discrete fiber lengths over 1 mm is not common. This may be due to longer fibers being more prone to clogging narrow nozzles or causing inconsistencies in filament diameter during processing. Continuous filament technology can address these challenges, and the 3D printing of composites with fiber lengths exceeding 1 mm remains an active area of research [35].

3.2 Fiber content-dependent fiber orientation

Figure 5 shows the fiber orientation distribution of the basalt fiber-reinforced composites. The orientation was determined with microtomography measurements. The distributions show the planar orientation in the (x, y) plane, and Fig. 5c shows the main diagonal components of the second-order fiber orientation tensor (A_{ij}) as a function of fiber content. In the tensor, a_{yy} indicates the direction parallel to the printing direction, a_{xx} is the direction perpendicular to it, and a_{zz} indicates the out-of-plane direction. The results show that as fiber content increases, the number of fibers aligned in the printing direction decreases. Shahzad et al. [36] found a similar relationship between fiber content and fiber orientation for 3D printing of steel fiber-reinforced concrete. At low fiber contents, fibers are well-dispersed and predominantly align with the shear flow in the nozzle. With increasing fiber content, the probability of fiber interactions increases, which leads to entanglement and randomization. With a higher fiber content, the melt viscosity of the composite is also higher, so there is less shear force within the melt [37, 38]. Based on the results, a linear relationship can be established between the main diagonal components and the fiber content (Eq. 20). Table 1 shows the fitted parameters (c_1, c_2) and the coefficient of determination (R^2).

Table 1 Parameters of the linear relationship fitted to fiber-content-dependent main diagonal components and the coefficient of determination

a_n	c_1	c_2	R^2
a_{xx}	0.002	0.11	1
a_{yy}	− 0.004	0.81	0.7246
a_{zz}	0.002	0.07	0.8372

$$a_n = c_1 w_f + c_2; 0 \le a_n \le 1 \tag{20}$$

where w_f (-) is the fiber weight fraction, and c_1 (-) and c_2 (-) are fitted constants. A linear approximation was used because, within the examined range of fiber content, the main diagonal components of the orientation tensor exhibited an approximately monotonic trend.

The fiber orientation has a significant effect on the mechanical properties, especially on the tensile strength. Therefore, the fiber orientation is often considered in predictive calculations using the orientation distribution function in the (x, y) plane. Based on the work of Li et al. [29], the fiber orientation correction factor (χ_2) can be calculated by Eq. 11. However, this requires knowledge of the orientation distribution in the product, which can be acquired by measurement or simulation. Both are time- and resource-intensive. Using Eq. 20, a novel method is presented to calculate the correction factor using the main diagonal components (Eq. 21) with the following assumptions: the y-axis is parallel to the 3D printing direction; the fiber orientation distribution in the (x, y) plane is symmetric to the y axis, and there is a linear relationship between the main diagonal components and the fiber weight fraction defined by Eq. 20. Then, the orientation correction factor ($\chi_{2,s}$) can be calculated with Eq. 21.

$$\begin{aligned}\chi_{2,s} = &\left(\left(a_{xx}cos\theta_x + a_{yy}cos\theta_y\right)\left(a_{xx}(cos^3\theta_x - \nu_{xy}sin^2\theta_x cos\theta_x) + a_{yy}(cos^3\theta_y - \nu_{xy}sin^2\theta_y cos\theta_y)\right)\right)\\ &\left(\left(a_{zz}cos\theta_z + a_{yy}cos\theta_y\right)\left(a_{zz}(cos^3\theta_z - \nu_{zy}sin^2\theta_z cos\theta_z) + a_{yy}(cos^3\theta_y - \nu_{zy}sin^2\theta_y cos\theta_y)\right)\right); 0 \le \chi_{2,s} \le 1\end{aligned} \tag{21}$$

where a_{xx}, a_{yy}, and a_{zz} are the main diagonal components of the orientation tensor in x, y, and z direction, respectively. $\theta_x = 90°$, $\theta_z = 90°$, and $\theta_y = 0°$ are the angles corresponding to the x, z, and y axes, respectively, interpreted in the (x,

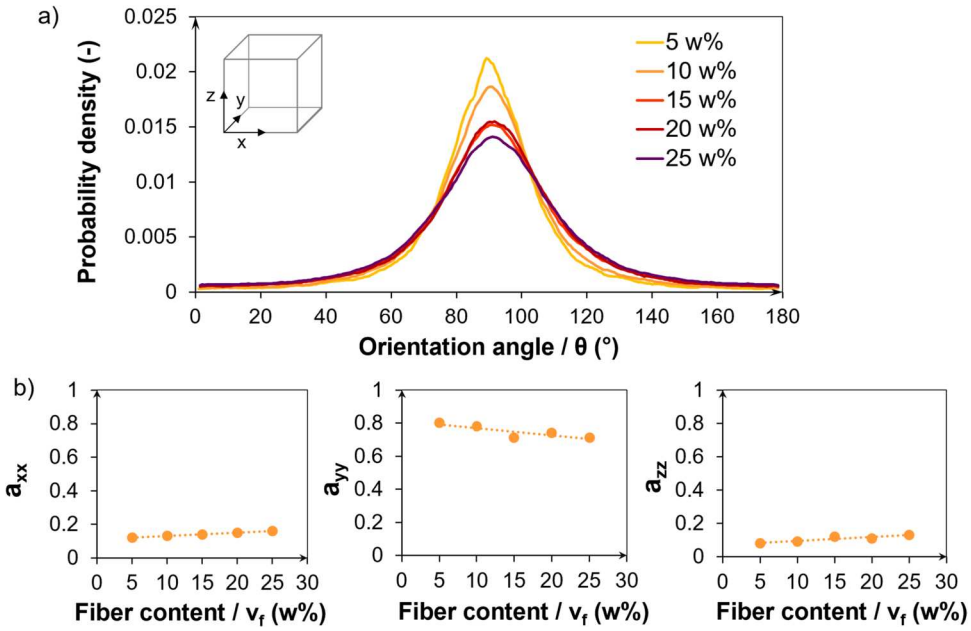

Fig. 5 **a** Fiber orientation distribution and **b** the main diagonal components of the orientation tensor as a function of fiber content

y) and (y, z) planes. $v_{xy} = 0.33$ is the major Poisson's ratio (relating contraction perpendicular to the fibers as a result of extension parallel to the fibers). In the case of perfect orientation in the printing direction, i.e., $a_{xx} = 0$ and $a_{yy} = 1$, $\chi_{2,s} = 1$. If the fiber orientation is uniform, i.e., the composite is perfectly isotropic in the (x, y) plane, $\chi_{2,s} = 0$.

3.3 Micromechanical modeling of tensile properties

Figure 7 shows experimental in-plane tensile strength and Young's modulus, and the results of the estimations based on the rule of mixtures (RoM) and the Halpin–Tsai (H-T) method. The stress–strain curves can be found in the Appendix (Fig. 9). The estimates were calculated for the discrete fiber contents examined (5–25 w%). Halpin–Tsai-based models for tensile strength (Eq. 22) and for Young's modulus (Eq. 23) are also proposed using the novel fiber orientation correction ($\chi_{2,s}$) factor (presented in Sect. 3.2). Table 3 (in the Appendix) contains the input parameters used for the modeling.

For tensile strength, the model parameters remain unchanged. For Young's modulus, the modified model integrates the orientation correction factor in a way that accounts for reinforcement efficiency in the denominator.

$$\sigma_{HT} = \chi_1 \chi_{2,s} \sigma_f w_f + w_m \sigma_m \tag{22}$$

$$E_{HT2} = E_m \left(\frac{1 + \xi \eta w_f}{1 - \chi_{2,s} \eta w_f} \right) \tag{23}$$

As expected, RoM vastly overestimates the tensile strength and Young's modulus. Microstructural properties such as fiber orientation, length, and fiber-matrix adhesion directly affect tensile strength and Young's modulus by determining how efficiently stress is transferred from the matrix to the fibers. Defects such as voids and agglomerations act as stress concentrators, leading to premature failure and reducing overall strength. These stochastic defects are very difficult to estimate; therefore, RoM model predictions are likely to be inaccurate. Naranjo-Lozada et al. [39] applied a RoM-based method to predict the elastic modulus of carbon fiber-reinforced polyamide composites. The authors found that the accuracy of the predictions decreased with increasing fiber volume fraction.

In the case of strength estimation, Eq. 22 was applied with orientation correction only ($\chi_1 = 1, \chi_{2,s} \neq 1$) and with fiber length and orientation correction as well ($\chi_1 \neq 1, \chi_{2,s} \neq 1$). The goodness of the model's predictions were rated by the percent error (δ) defined by Eq. 16. Figure 6a shows a systematic analysis of the effect of χ_1 and χ_2. Starting from the simplest case, RoM, which does not take either factor into account, to the proposed model, which accounts for both. For the five examined cases, the mean error of the proposed model containing both the length and orientation correction is 18%. The maximum error value is 34% for 10 w% fiber content, and the minimum error is 6% for 5 w% and 15 w%. Thus, in the 5 and 15 wt% cases, this approach can give a quite accurate estimate with an error of only 6%. Overall, the proposed model can be used as an approximation. Note

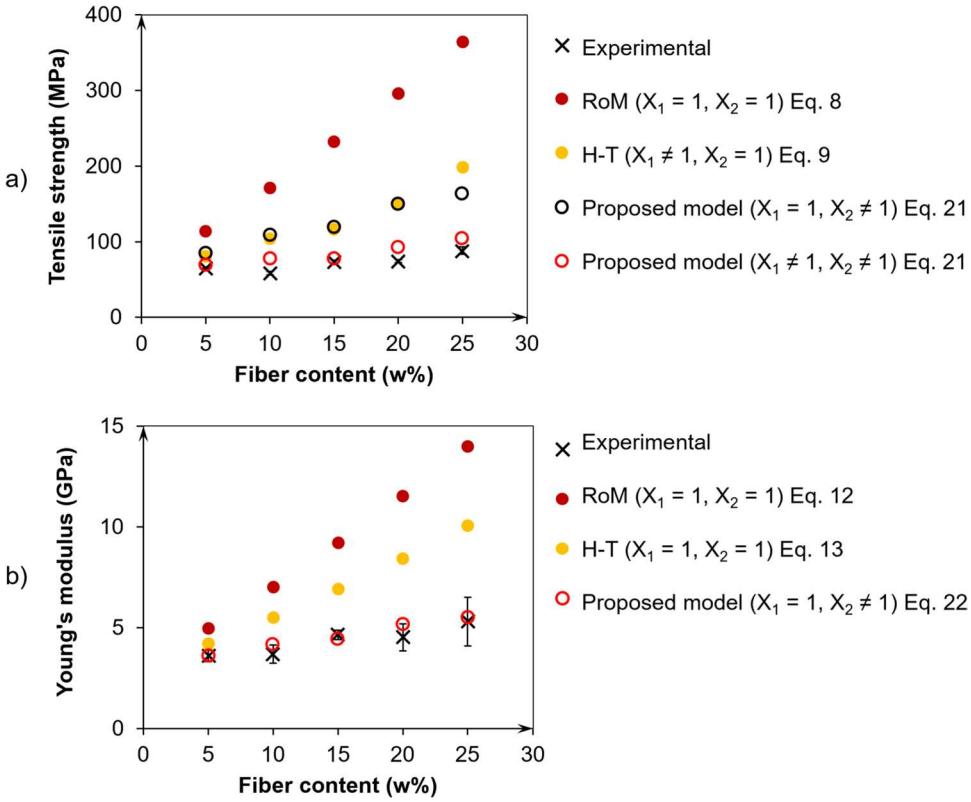

Fig. 6 **a**) In-plane tensile strength and **b**) Young's modulus of the basalt fiber-reinforced composites as a function of fiber content

that without the measurement-based length correction, the mean error of the prediction is 73%, and the individual errors are between 31 and 102%. Figure 6a and Table 2 reveal that when comparing H-T (which considers only the effect of χ_1) to the proposed model considering the effect of χ_2, the model accounting for χ_2 produced more accurate results. This indicates that the influence of fiber orientation (χ_2) is more significant than the effect of fiber length (χ_1). Furthermore, applying the proposed fiber orientation correction factor ($\chi_{2,s}$) greatly improves the accuracy of the tensile strength prediction.

In the case of Young's modulus, the modeling accuracy can be significantly enhanced by incorporating the effect of fiber orientation (χ_2) into the H-T model. For the five examined cases, the mean error of the proposed model containing both the length and orientation correction is only 7%. The maximum error value is 14%, and the minimum error is 0%. In three of the five cases, the percent error of the modeling was below 5%. These results suggest that the modified Halpin–Tsai model we proposed is highly effective for predicting Young's modulus of short-fiber thermoplastic composites. Considering fiber content, both the RoM and H-T models predict a substantial linear increase, whereas experimental results show only a modest linear trend.

We compared our results with other analytical models from the literature that predict the tensile properties of short fiber-reinforced 3D-printed composites. The Eshelby-Mori–Tanaka model integrates Eshelby's solution for ellipsoidal inclusion with Mori–Tanaka's method for averaging local stresses to predict the effective elastic properties. While the Eshelby-Mori–Tanaka model takes into account the interactions between inclusions and the surrounding matrix, the Halpin–Tsai model offers an empirical approach based on the fitting of parameters to experimental data, and provides simpler but less sensitive predictions [40, 41]. Shirasu et al. [42] applied a two-scale micromechanics model based on the Eshelby-Mori–Tanaka approach to predict the stress–strain behavior by incorporating void volume fraction, fiber length, and fiber orientation distribution. The authors demonstrated that the Mori–Tanaka method can be effectively used for rapid estimation of equivalent stiffness and elastoplastic behavior, and that it requires significantly less computation time than finite element analysis.

3.4 3D anisotropy

The 3D anisotropy of the composite structures was characterized using the anisotropy ratios defined by Eqs. 17–19 (Fig. 7). Table 4 (in the Appendix) contains the input parameters used for the calculations. The rate of anisotropy for all tensile properties increased parabolically with increasing fiber content, with a local maximum at 10–15 w%. This indicates that the difference between in-plane and interlayer

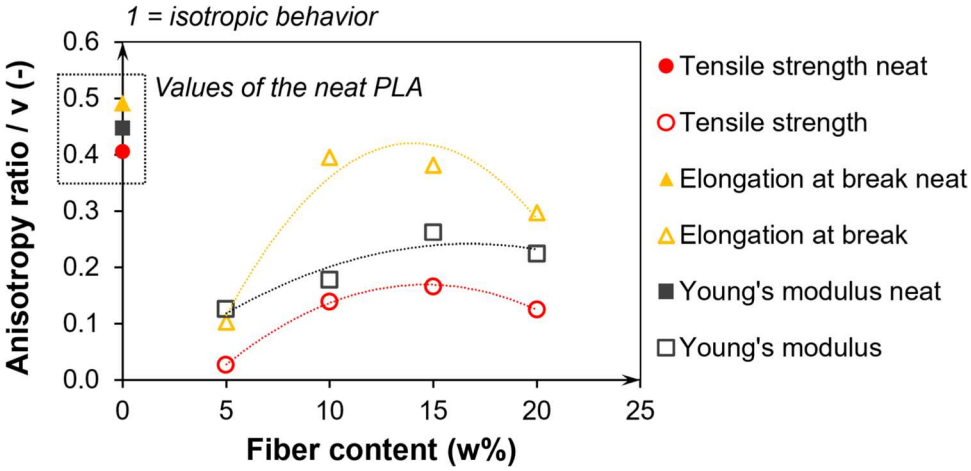

Fig. 7 Anisotropy ratios of the tensile properties as a function of fiber content

Table 2 Error of the micromechanical modeling in the case of Young's modulus and tensile strength prediction

Fiber content (w%)	Error of modeling (%)						
	Tensile strength				Young's modulus		
	RoM	H-T	Proposed model ($\chi_1 = 1$, χ_2)	Proposed model ($\chi_1 \neq 1$, $\chi_2 \neq 1$)	RoM	H-T	**Proposed model** ($\chi_1 = 1$, χ_2)
5	75	23	31	6	38	17	0
10	193	77	86	34	91	49	12
15	215	59	63	6	99	49	5
20	299	103	102	24	155	86	14
25	312	124	85	18	164	90	4

properties is smallest at these fiber contents, so the composite shows isotropic behavior under tensile loading. The anisotropy ratio is the smallest in the case of tensile strength. Since strength is a failure property, it depends most on microstructural characteristics. Fibers aligned in the load direction will exert reinforcement. Therefore, the in-plane strength should increase. However, the interlayer strength is governed by the fiber-matrix interfaces, as it was shown that fiber orientation in the z direction is the least prominent (Fig. 5) [23]. Therefore, the directional dependence is strongest for tensile strength. No significant difference is observed for Young's modulus as a function of fiber content. When compared to the unreinforced PLA, composites show a higher degree of anisotropy. This may be due to weaker interlayer polymer bonding, as weak chain entanglement can result in weaker modulus. Lastly, the anisotropy ratio was the closest to that of the neat PLA for the elongation at break. In general, the elongation at break of short fiber-reinforced composites decreases with increasing fiber content, due to the brittle fibers. In our previous research, it was shown that the interfacial shear strength (τ) for basalt fiber-reinforced PLA is $\tau = 10.4$ MPa [20]. For higher τ values, better load transfer can be expected, but the elongation of the matrix is limited by the fibers. Thus, the elongation of the fibers determines the mechanical response of the composite.

Anisotropy, when its extent and formation mechanisms are known, can greatly assist in creating heterogeneous materials with tailored properties. Sadeghi et al. [43] found architecture-dependent strengthening mechanisms in graphite/aluminum lamellar composites, and a model for designing high-strength composites was proposed. Although both architected heterogeneous composites and short fiber-reinforced 3D-printed composites exhibit anisotropy and architecture-dependent strengthening, the underlying mechanisms and control over mechanical performance differ. However, there are promising opportunities to fuse ideas from these fields. The deliberate, hierarchical microstructural engineering strategies used in architected composites could inspire more advanced 3D printing design methodologies, such as controlled fiber placement or multi-material printing at the filament scale.

For the analysis of anisotropy, SEM images of the fracture surfaces were also taken after the in-plane and interlayer tensile tests. Figure 8 shows the micrographs for the lowest (5 w%) and the highest (25 w%) fiber contents. Consistent

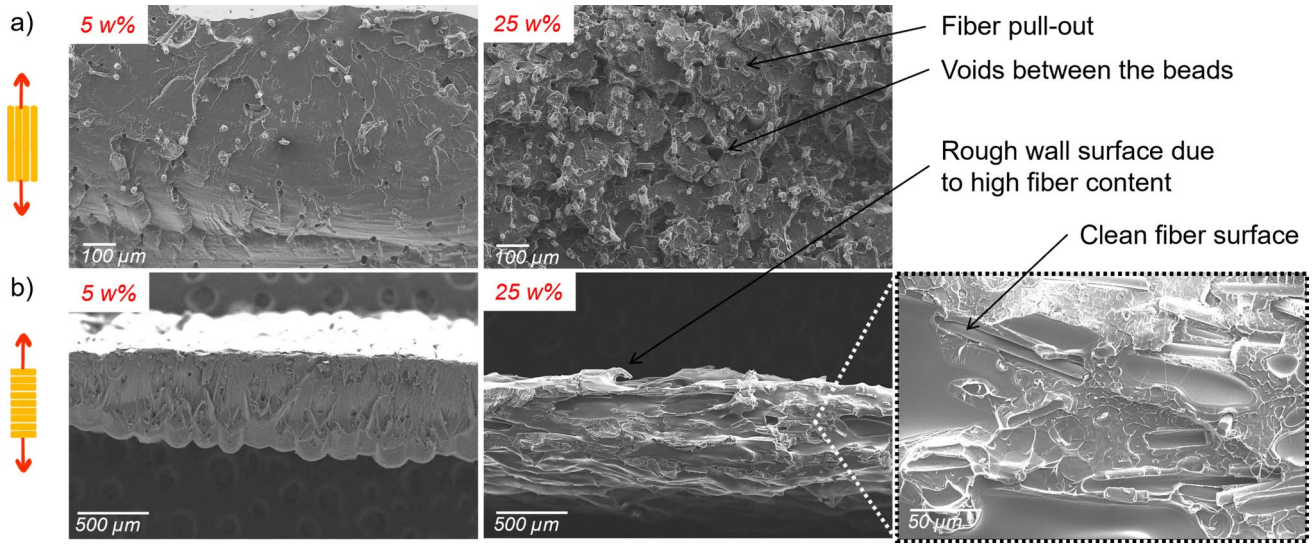

Fig. 8 Scanning electron microscopy images taken after failure in the case of the (**a**) in-plane and the (**b**) interlayer test specimens

with the micro-CT results, the majority of the fibers are oriented parallel to the printing direction. Traces of fiber pull-out can be observed in the in-plane samples, indicating an inadequate fiber-matrix relationship. Clean fiber surfaces are also observed after interlayer tests. In the composite with the highest fiber content (25 w%), small voids appear, which may be due to the reduced flowability caused by the fibers.

4 Conclusion

In this study, the applicability of micromechanical models for short fiber-reinforced 3D-printed composites was investigated. Basalt fiber-reinforced poly(lactic acid) filaments were prepared with fiber contents between 5 and 25 w%. Microstructural measurements were used to determine fiber length and fiber orientation factor. Via micro-computed tomography analysis, a linear correlation was identified between fiber content and fiber orientation, based on which a method was proposed for estimating the fiber orientation correction factor. The use of orientation correction enables the prediction of Young's modulus and tensile strength while reducing the number of measurements required. For the five examined cases, the mean error of the proposed model for Young's modulus and tensile strength were 7% and 18%, respectively. The obtained results suggest that the modified Halpin–Tsai model we proposed is highly effective for predicting Young's modulus of short-fiber thermoplastic composites. The anisotropy ratio was also introduced as a dimensionless parameter to quantify the orientation dependence of tensile properties. Our results show that the isotropic behavior can be best approximated at a fiber content of 15 w%. 3D-printed fiber-reinforced composites are typically used in structures of non-negligible thickness; therefore, understanding the anisotropy is key to designing parts subjected to complex loading conditions. The results of this study will contribute to improving the predictability of the mechanical properties of 3D-printed fiber-reinforced composites, thus helping to optimize their design for practical applications.

Appendix

Table 3 Input parameters for the RoM, H-T, and the proposed model for predicting in-plane properties

Fiber content (w%)	σ_{fiber} (MPa)	σ_{matrix} (MPa)	E_{fiber} (MPa)	E_{matrix} (MPa)	χ_1 (-)	$\chi_{2,s}$ (-)	η(-)	ξ(-)
5	2335	60	85,000	3000	0.398	0.48	0.39	41.67
10					0.409	0.45		
15					0.349	0.36		
20					0.400	0.40		
25					0.468	0.36		

Table 4 Input parameters for calculating the anisotropy ratios (ϑ_σ, ϑ_E, ϑ_ε)

Fiber content (w%)	σ_{xy} (MPa)	E_{xy} (MPa)	ε_{xy} (-)	σ_z (MPa)	E_z (MPa)	ε_z (-)
5	65.4	3595	4.36	1.7	452.0	0.45
10	58.6	3683	4.13	8.1	652.6	1.63
15	73.7	4640	4.02	12.2	1215.6	1.53
20	74.4	4520	4.16	9.3	1011.4	1.24

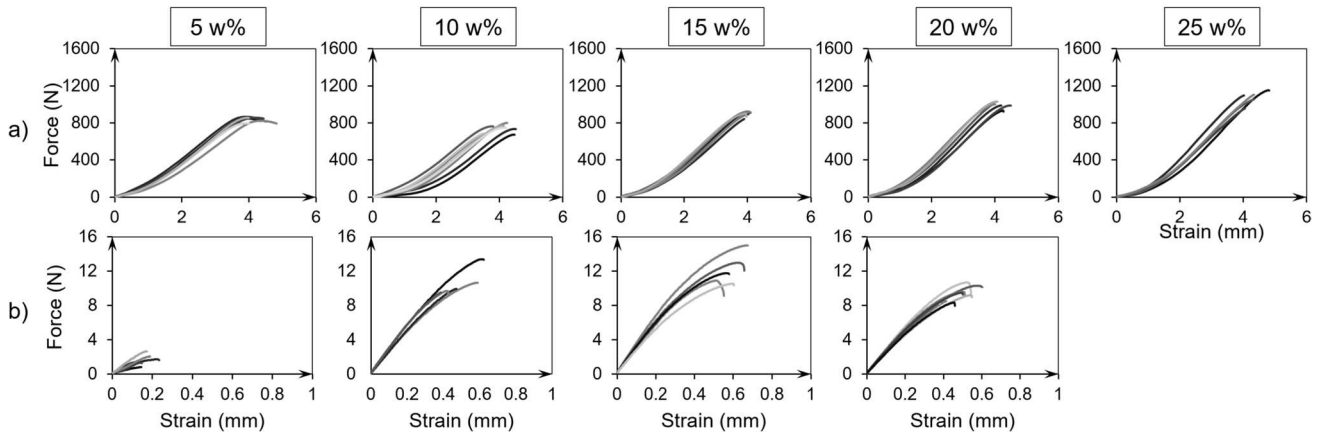

Fig. 9 Tensile stress–strain curves obtained with (**a**) in-plane and (**b**) interlayer tensile tests

Acknowledgements The authors are grateful for all the colleagues of Elas Kft. for their help in performing the micro-computed tomography measurements.

Author contribution The authors contributed to conceptualization and methodology equally. Investigation, visualization, and writing the original draft were performed by Csenge Tóth. Formal analysis, validation, and review and editing were performed by Ábris Dávid Virág.

Funding Open access funding provided by Budapest University of Technology and Economics. Project no. TKP-6–6/PALY-2021 has been implemented with the support provided by the Ministry of Culture and Innovation of Hungary from the National Research, Development, and Innovation Fund, financed under the TKP2021-NVA funding scheme. Csenge Tóth is thankful for the support of the EKÖP-24–4-I-BME-198 University Research Fellowship Programme of the Ministry for Culture and Innovation from the source of the National Research, Development, and Innovation Fund. Ábris Dávid Virág is thankful for the support of the EKÖP-24–4-I-BME-201 University Research Fellowship Programme of the Ministry for Culture and Innovation from the source of the National Research, Development, and Innovation Fund. The research reported in this paper was supported by the National Research, Development, and Innovation Office (NRDI, Hungary) through grants K146236.

Declarations

Conflict of interest The authors declare no competing interests.

References

1. Mushtaq RY, Ahmad A, Abdul Khalil HPS et al (2024) Elucidating the synergistic interactions of macroalgae and cellulose nanofibers on the 3D structure of composite bioaerogel properties. Express Polym Lett 18:760–777. https://doi.org/10.3144/expresspolymlett.2024.56
2. da Siqueira A, S, Braga NF, Muñoz PAR, et al (2024) Biodegradable scaffold: integration of polylactic acid, hydroxyapatite, and graphene oxide via FDM 3D printing. Express Polym Lett 18:656–672. https://doi.org/10.3144/expresspolymlett.2024.48
3. Lei M, Wang Y, Wei Q et al (2023) Micromechanical modeling and numerical homogenization calculation of effective stiffness of 3D printing PLA/CF composites. J Manuf Process 102:37–49. https://doi.org/10.1016/j.jmapro.2023.07.027
4. Sayah N, Smith DE (2022) Effect of process parameters on void distribution, volume fraction, and sphericity within the bead microstructure of large-area additive manufacturing polymer composites. Polymers (Basel) 14:. https://doi.org/10.3390/polym14235107
5. Pei S, Wang K, Chen C-B et al (2021) Process-structure-property analysis of short carbon fiber reinforced polymer composite via fused filament fabrication. J Manuf Process 64:544–556. https://doi.org/10.1016/j.jmapro.2021.02.019
6. Ficzere P (2024) Surface anisotropy on 3D printed parts. Periodica Polytechnica Mechanical Engineering 68:272–277. https://doi.org/10.3311/PPme.37770
7. Mulholland T, Goris S, Boxleitner J, et al (2018) Process-induced fiber orientation in fused filament fabrication. Journal of Composites Science 2:. https://doi.org/10.3390/jcs2030045
8. Aurich T, Mennig G (2001) Flow-induced fiber orientation in injection molded fit fiber reinforced polypropylene. Polym Compos 22:680–689. https://doi.org/10.1002/pc.10570
9. Dupuis A, Pesce JJ, Ferreira P, Régnier G (2020) Fiber orientation and concentration in an injection-molded ethylene-propylene copolymer reinforced by hemp. Polymers (Basel) 12:1–20. https://doi.org/10.3390/polym12122771
10. Consul P, Beuerlein KU, Luzha G, Drechsler K (2021) Effect of extrusion parameters on short fiber alignment in fused filament fabrication. Polymers (Basel) 13:. https://doi.org/10.3390/polym13152443
11. Yan J, Demirci E, Ganesan A, Gleadall A (2022) Extrusion width critically affects fibre orientation in short fibre reinforced material extrusion additive manufacturing. Addit Manuf 49:102496. https://doi.org/10.1016/j.addma.2021.102496
12. Shulga E, Karamov R, Sergeichev IS, et al (2020) Fused filament fabricated polypropylene composite reinforced by aligned glass fibers. Materials 13:. https://doi.org/10.3390/MA13163442
13. Yu S, Hwang YH, Lee KT et al (2022) Outstanding strengthening and toughening behavior of 3D-printed fiber-reinforced composites designed by biomimetic interfacial heterogeneity. Advanced Science 9:2103561. https://doi.org/10.1002/advs.202103561
14. Papon EA, Haque A, Spear SK (2020) Effects of functionalization and annealing in enhancing the interfacial bonding and mechanical properties of 3D printed fiber-reinforced composites. Mater Today Commun 25:101365. https://doi.org/10.1016/j.mtcomm.2020.101365
15. Allum J, Moetazedian A, Gleadall A, Silberschmidt VV (2020) Interlayer bonding has bulk-material strength in extrusion additive manufacturing: new understanding of anisotropy. Addit Manuf 34:101297. https://doi.org/10.1016/j.addma.2020.101297
16. König M, Diekmann J, Lahres M, Middendorf P (2022) Experimental investigation of process-structure effects on interfacial bonding strength of a short carbon fiber/polyamide composite fabricated by fused filament fabrication. Progress in Additive Manufacturing 7:593–607. https://doi.org/10.1007/s40964-021-00249-4
17. Bhandari S, Lopez-Anido RA, Gardner DJ (2019) Enhancing the interlayer tensile strength of 3D printed short carbon fiber reinforced PETG and PLA composites via annealing. Addit Manuf 30:100922. https://doi.org/10.1016/j.addma.2019.100922
18. Dhand V, Mittal G, Rhee KY et al (2015) A short review on basalt fiber reinforced polymer composites. Compos B Eng 73:166–180. https://doi.org/10.1016/j.compositesb.2014.12.011
19. Chen X, Li Y, Gu N (2010) A novel basalt fiber-reinforced polylactic acid composite for hard tissue repair. Biomed Mater 5:044104. https://doi.org/10.1088/1748-6041/5/4/044104
20. Tóth C, Kovács NK (2022) Comparison of the accuracy of analytical models for basalt fiber–reinforced poly(lactic acid) composites prepared by injection molding and fused filament fabrication. Int J Adv Manuf Technol 121:3999–4010. https://doi.org/10.1007/s00170-022-09572-8

21. Fu SY, Lauke B, Mäder E et al (2000) Tensile properties of short-glass-fiber- and short-carbon-fiber-reinforced polypropylene composites. Compos Part A Appl Sci Manuf 31:1117–1125. https://doi.org/10.1016/S1359-835X(00)00068-3
22. Tábi T, Gere D, Csézi G, Pölöskei K (2024) Influence of epoxidized natural rubber of the thermoformability of poly(lactic acid) biopolymer films using elevated temperature ball burst tests. J Therm Anal Calorim 149:75–87. https://doi.org/10.1007/s10973-023-12712-1
23. Tóth C, Lukács NL, Kovács NK (2024) The role of the fiber–matrix interface in the tensile properties of short fiber–reinforced 3D-printed polylactic acid composites. Polym Compos. https://doi.org/10.1002/pc.28720
24. Sadeghi B, Cavaliere PD (2023) Reviewing the integrated design approach for augmenting strength and toughness at macro- and micro-scale in high-performance advanced composites. Materials 16
25. Lubineau G, Alfano M, Tao R, et al (2024) Harnessing extrinsic dissipation to enhance the toughness of composites and composite joints: a state-of-the-art review of recent advances. Advanced Materials
26. Fu S-Y, Lauke B, Mai Y-W (2009) Major factors affecting the performance of short fibre reinforced polymers. Science and Engineering of Short Fibre Reinforced Polymer Composites 29–58. https://doi.org/10.1533/9781845696498.29
27. Durin A, De Micheli P, Ville J et al (2013) A matricial approach of fibre breakage in twin-screw extrusion of glass fibres reinforced thermoplastics. Compos Part A Appl Sci Manuf 48:47–56. https://doi.org/10.1016/j.compositesa.2012.12.011
28. Inceoglu F, Ville J, Ghamri N et al (2011) Correlation between processing conditions and fiber breakage during compounding of glass fiber-reinforced polyamide. Polym Compos 32:1842–1850. https://doi.org/10.1002/pc.21217
29. Li Y, Li W, Deng Y et al (2018) Temperature-dependent longitudinal tensile strength model for short-fiber-reinforced polymer composites considering fiber orientation and fiber length distribution. J Mater Sci 53:12190–12202. https://doi.org/10.1007/s10853-018-2517-8
30. Yu S, Hwang YH, Hwang JY, Hong SH (2019) Analytical study on the 3D-printed structure and mechanical properties of basalt fiber-reinforced PLA composites using X-ray microscopy. Compos Sci Technol 175:18–27. https://doi.org/10.1016/j.compscitech.2019.03.005
31. Zhou D, Tong X, Liu H, et al (2024) A modified Halpin-Tsai model for predicting the elastic modulus of composite materials. AIP Adv 14:. https://doi.org/10.1063/5.0160256
32. Nasirov A, Gupta A, Hasanov S, Fidan I (2020) Three-scale asymptotic homogenization of short fiber reinforced additively manufactured polymer composites. Compos B Eng 202:108269. https://doi.org/10.1016/J.COMPOSITESB.2020.108269
33. Kim Y, Park OO (2020) Effect of fiber length on mechanical properties of injection molded long-fiber-reinforced thermoplastics. Macromol Res 28:433–444. https://doi.org/10.1007/s13233-020-8056-6
34. Yan X, Cao S (2018) Structure and interfacial shear strength of polypropylene-glass fiber/carbon fiber hybrid composites fabricated by direct fiber feeding injection molding. Compos Struct 185:362–372. https://doi.org/10.1016/j.compstruct.2017.11.037
35. van de Werken N, Tekinalp H, Khanbolouki P et al (2020) Additively manufactured carbon fiber-reinforced composites: state of the art and perspective. Addit Manuf 31:100962. https://doi.org/10.1016/j.addma.2019.100962
36. Shahzad Q, Abbas N, Akbar M, et al (2024) Influence of print speed and nozzle diameter on the fiber alignment in 3D printed ultra-high-performance concrete. Front Mater 11:. https://doi.org/10.3389/fmats.2024.1355647
37. Asoodeh F, Aghvami-Panah M, Salimian S et al (2022) The effect of fibers' length distribution and concentration on rheological and mechanical properties of glass fiber–reinforced polypropylene composite. J Ind Text 51:8452S-8471S. https://doi.org/10.1177/15280837211043254
38. Pu L, Xu P, Xu M et al (2021) Effect of fiber on rheological properties and flow behavior of polymer completion fluids. ACS Omega 6:17136–17148. https://doi.org/10.1021/acsomega.0c05346
39. Naranjo-Lozada J, Ahuett-Garza H, Orta-Castañón P et al (2019) Tensile properties and failure behavior of chopped and continuous carbon fiber composites produced by additive manufacturing. Addit Manuf 26:227–241. https://doi.org/10.1016/j.addma.2018.12.020
40. Mishra N, Das K (2020) A Mori–Tanaka based micromechanical model for predicting the effective electroelastic properties of orthotropic piezoelectric composites with spherical inclusions. SN Appl Sci 2:. https://doi.org/10.1007/s42452-020-2958-y
41. Tóth C, Molnár K, Virág ÁD (2025) Short fiber reinforcement in material extrusion 3D printing: a meta-analysis review with insights into sustainable alternatives. Polym Compos. https://doi.org/10.1002/pc.29850
42. Shirasu K, Yamaguchi Y, Hoshikawa Y et al (2024) Micromechanics study of short carbon fiber-reinforced thermoplastics fabricated via 3D printing using design of experiments. Mater Sci Eng, A 891:145971. https://doi.org/10.1016/j.msea.2023.145971
43. Sadeghi B, Cavaliere P, Pruncu CI (2022) Architecture dependent strengthening mechanisms in graphene/Al heterogeneous lamellar composites. Mater Charact 188:111913. https://doi.org/10.1016/j.matchar.2022.111913